Journal of Materials Chemistry C

Accepted Manuscript

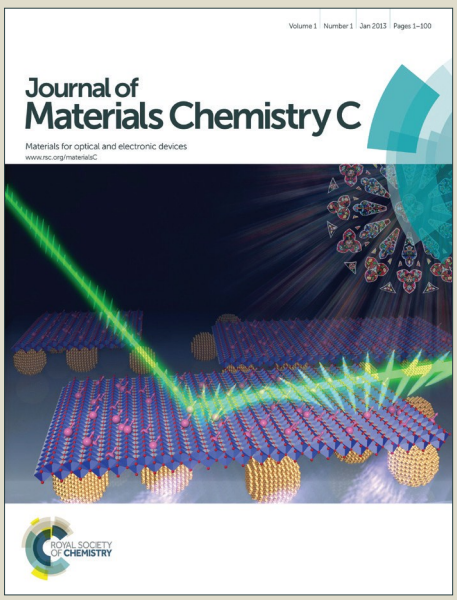

ROYAL SOCIETY OF CHEMISTRY

www.rsc.org/materialsC

Luminescent properties of europium-doped $(H_3O)Y_3F_{10} \cdot xH_2O$ nanocrystals

Cyril Caron, Denis Boudreau and Anna M. Ritcey

Department of Chemistry, Centre d'optique, photonique et laser (COPL) and Centre de recherche sur les matériaux avancés (CERMA), Université Laval, Québec, Canada, G1V 0A6

Abstract

Low-polydispersity europium-doped $(H_3O)Y_3F_{10} \cdot xH_2O$ single-crystal nanoparticles can be prepared via a simple reverse microemulsion method. The doping level of the particles can be varied by changing the relative concentration of europium to yttrium in the initial precursor mixture. Doping levels of up to 14 ± 2 at% can be attained without loss of the host crystal structure. Final europium concentrations, however, fall below those of the precursor solutions, suggesting that europium ions are less readily incorporated into the $(H_3O)Y_3F_{10} \cdot xH_2O$ crystal lattice than are yttrium ions. Emission spectra of the doped nanoparticles show sharp well-defined lines, which can be assigned to known europium transitions. The emission intensity increases linearly with increasing europium content. Europium ions within the nanocrystals exhibit excited-state lifetimes of 3 - 5 ms. These values are an order of magnitude greater than those of free ions in solution, indicating that ion incorporation in the yttrium fluoride matrix efficiently reduces non-radiative energy losses. Finally, data from time-resolved phosphorescence measurements suggests that europium ions within the particles are located in spectroscopically different environments which can be tentatively assigned to surface and core sites.

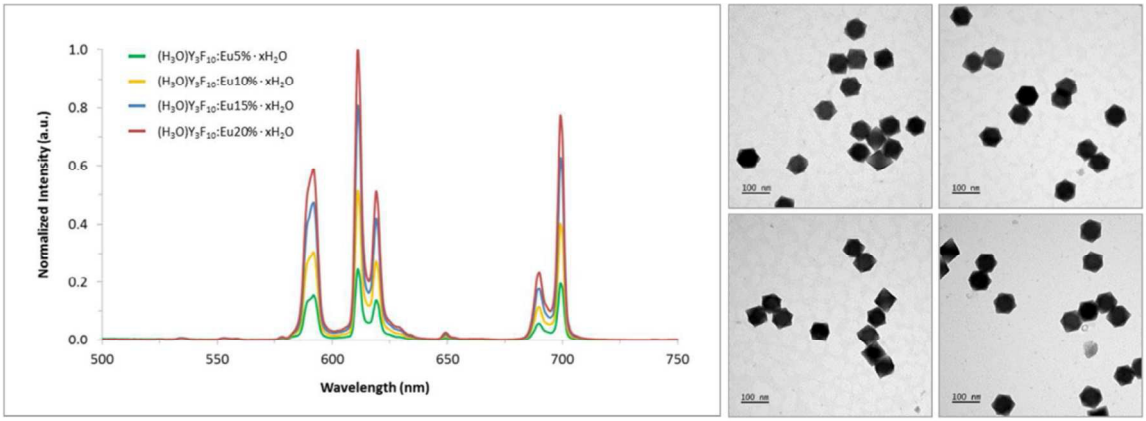

Keywords

Luminescent probes, Lanthanides, Yttrium fluoride, Steady-state and time-resolved phosphorescence spectroscopy, Time-correlated single photon counting

1. Introduction

The unique spectral properties of lanthanides make these elements very attractive tools for many fields of research, including biosensing and medical imaging.[1] Luminescent probes employing lanthanides, for example, offer significant advantages when compared to conventional organic luminescent probes. Indeed, lanthanide-based probes are known to display better photostability, narrower emission bandwidths and higher Stokes shifts, while their millisecond-range excited-state lifetimes allow the use of gated detection techniques to increase signal/noise ratios.[2] One frequently employed strategy for the development of such probes is the incorporation of lanthanide ions or complexes into nanoscopic entities (i.e. nanoparticles). In this way, the luminescent agents are protected from the external environment and its quenching effects. Furthermore, since a large number of the emitters can usually be incorporated into a single nanoparticle, higher signal intensities and improved detection limits can be obtained when using these particles as labels or probes.

Many different host matrices have been employed for the synthesis of such nanomaterials. Choosing one over the other generally depends on the desired properties and the targeted application. Among the materials that may be used for the preparation of lanthanide-doped luminescent probes, lanthanide oxides[3,4,5] and fluorides[6,7,8,9] are the most common. Yttrium fluoride, for example, has particularly interesting characteristics that make it a highly promising host for the development of lanthanide-doped luminescent probes. Firstly, rare earth fluoride crystals are generally characterized by lower lattice vibration frequencies than other materials, thus minimizing non-radiative energy loss through phonon interactions.[10] Secondly, yttrium and most lanthanides have, in their +3 oxidation state, similar atomic radii.[11] Relatively high doping levels can thus be achieved without alteration of the crystalline structure of the nanoparticles. Moreover, in the context of biological applications, high stability and low cytotoxicity are other features that are commonly sought.

There are many different examples of phosphorescent lanthanide-doped yttrium fluoride nanoparticles in literature.[12,13,14,15] Spectroscopic studies of these materials are of the utmost importance for the delineation of structure-property relationships and the subsequent development of greater efficiency probes. However, characterization of the spectral properties is often limited by poor control over critical parameters such as size, polydispersity or crystallinity of the nanoparticles. In this article, we report the synthesis and characterization of low-polydispersity, luminescent $(H_3O)Y_3F_{10} \cdot xH_2O$ single-crystal nanoparticles doped at 5%, 10%, 15% and 20% with europium ions. These phosphorescent yttrium fluoride nanoparticles are synthesized via a simple reverse microemulsion method that offers the facile modulation of particle size by varying the water/surfactant molar ratio.[16] A schematic representation of the different processes involved in the synthesis of the $(H_3O)Y_3F_{10} \cdot xH_2O$ single-crystal nanoparticles by the reverse microemulsion technique is presented in Figure 1. A discussion of the mechanisms involved in the formation of the nanoparticles[17] and details concerning their crystal structure[18] have been published elsewhere. In the present paper, the spectral properties of these europium-doped nanoparticles are investigated by steady-state and time-resolved phosphorescence spectroscopy. In order to establish the relationship between these properties and the structure of the nanocrystals, the particles are also characterized by transmission electron microscopy (TEM), thermogravimetric analysis (TGA), energy-dispersive X-ray (EDX) spectroscopy and inductively coupled plasma mass spectrometry (ICP-MS).

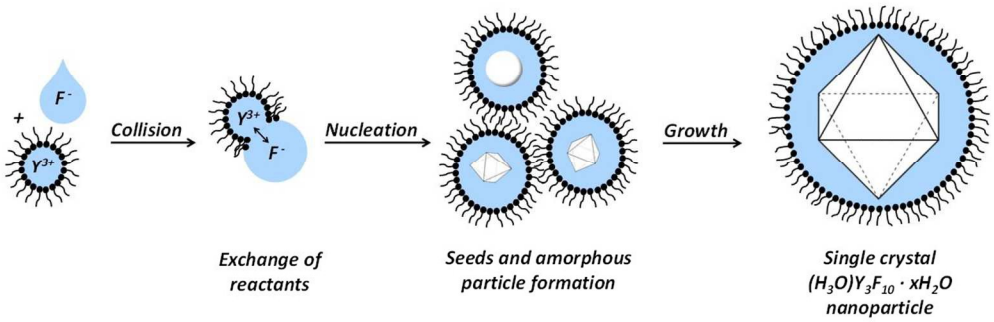

Figure 1 : Schematic representation of the different processes involved in the synthesis of $(H_3O)Y_3F_{10} \cdot xH_2O$ single-crystal nanoparticles by the reverse microemulsion technique. The drawing is not to scale.

2. Materials and methods

2.1 Materials

All chemicals were purchased from Sigma-Aldrich and used as received unless otherwise specified. Aqueous solutions employed in the synthesis of the nanoparticles were prepared with deionized water of nanopure quality (17.8 - 18.1 Mohms resistivity). Yttrium chloride hexahydrate and europium chloride hexahydrate salts were acquired with purities of 99.99% and 99.9% respectively, whereas ammonium hydrogen difluoride salt was purchased with purity equal or greater to 98%. ACS certified cyclohexane, supplied by Fisher Scientific, was used for the preparation of the microemulsions. Trace metal grade concentrated nitric acid, furnished by BDH Anistar Plus, was employed for the digestion of the nanoparticles. Yttrium, europium and praseodymium single element ICP calibration standards were provided by PlasmaCAL.

2.2 Synthesis of the luminescent europium-doped yttrium fluoride nanoparticles

The synthesis of low-polydispersity single-crystal yttrium fluoride nanoparticles was performed by slightly modifying a previously reported method using a reverse microemulsion.[16] The procedure consists of first dissolving 36 g of polyoxyethylene (5) nonylphenyl ether (Igepal CO-520) and 4 g of sodium bis(2-ethylhexyl) sulfosuccinate (AOT) in 300 mL of cyclohexane with magnetic stirring. A 10 mL aliquot of a 400 mM aqueous solution of yttrium chloride hexahydrate and europium chloride hexahydrate is then added. Different doping levels are obtained by varying the molar ratio of the europium and yttrium chlorides in this solution. The total molar concentration (yttrium + europium), however, remains constant at 400 mM in order to maintain an equivalent amount of reagent from one synthesis to another. Here, europium doping levels of 5%, 10%, 15% and 20% are used. Following the addition of the first aqueous solution, the system is allowed to stabilize under continuous stirring for one hour to ensure the formation of uniform reverse micelles. Then, a 10 mL aliquot of a 400 mM ammonium hydrogen difluoride aqueous solution is added. The system is finally tightly sealed in order to avoid any loss of cyclohexane and the microemulsion is left to stir for one week. Any loss of solvent will result in an unwanted modification of the number and size of the reverse micelles and therefore have an impact on the outcome of the synthesis.

In this work, europium was selected as the dopant ion because of its excitation and emission peaks located in the visible part of the electromagnetic spectrum which greatly simplifies the equipment needed for the characterization of the spectral properties. Other lanthanide ions can, however, be introduced

through the same synthetic method, although the maximum doping level achievable without loss of the matrix crystal structure is specific to each lanthanide.

2.3 Purification of the luminescent europium-doped yttrium fluoride nanoparticles

Once the growth process is complete, the nanoparticles are purified by ultrafiltration with a 75 mL Millipore Solvent Resistant Stirred Cell and Ultracel PL-100 membranes (100 kDa NMWL), both provided by Millipore EMD. To proceed, the microemulsions containing the particles are first transferred to a rotary evaporator and the cyclohexane is completely removed. The resulting viscous mixtures are then redispersed in approximately 150 mL of methanol using an ultrasonic bath, passed through the ultrafiltration membrane and rinsed several times, within the filtration cell, with methanol. Once washed, the samples are removed from the cell, dried in a vacuum oven at 80 - 85 °C for at least 24 hours, cooled to room temperature and weighed. White nanoparticle powders with masses ranging from 250 to 500 mg were in this way recovered. In ascending order of doping, yields of 57%, 83%, 95% and 82% were obtained. The nanoparticles were stored under ambient conditions in screw-cap glass vials.

2.4 Characterization

Nanoparticle size was determined by transmission electron microscopy (TEM) using the image processing software Image-J. TEM images were recorded at 80 kV using a JEOL 1230 microscope equipped with an Ultrascan 1000XP high resolution CCD camera. To enable sample deposition, nickel TEM grids were first coated with a thin Formvar film on which a carbon layer was subsequently deposited. Nanoparticle suspensions were then prepared by dispersing 10 mg of purified sample in 10 mL of methanol using an ultrasonic bath. Small amounts of chloroform were next carefully poured onto the carbon-coated grids to remove the Formvar film. Two drops of nanoparticle suspension were deposited per grid and these were dried overnight at room temperature before being observed. Mean size values were determined by individually measuring more than one hundred nanoparticles.

The inorganic content of the nanoparticle powders isolated by ultrafiltration was determined by thermogravimetric analysis (TGA). For this purpose, a STA 449C Jupiter Thermo-microbalance coupled to a QMS 403 C Aeolos mass spectrometer gas analyzer was used. Both devices were purchased from Netzsch-Gerätebau GmbH. To perform the analyses, masses of 5.5 to 6.5 mg of purified sample were transferred to a Al_2O_3 crucible and heated from 35 to 600 °C at a rate of 10 °C/min with an air purge of 20 mL/min. Mass spectrometry (MS) analyses were performed simultaneously to the thermogravimetric measurements in order to further investigate the thermal decomposition of the samples. In this way, generation of decomposition products such as H_2O and CO_2 was followed during the complete heating process at mass-to-charge ratios (m/z) of 18 and 44, respectively (see supporting information Figure S2).

The europium content of the yttrium fluoride nanoparticles was determined by energy-dispersive X-ray spectroscopy (EDX). To this end, indium tin oxide covered microscope slides were first carefully washed and dried. Next, 100 µL of the same nanoparticle suspensions as those used for the preparation of TEM grids were spin-coated onto the slides. The energy-dispersive X-ray spectroscopy analysis was carried out on a Quanta 3D FEG scanning electron microscope from FEI equipped with the TEAM EDS Analysis System for SEM from EDAX. The elemental composition was measured twice for each sample by spotting the electron beam at 30 kV on two different nanoparticle aggregates of several microns in size. The mean doping level was then calculated for each sample using the Eu/Y atomic ratio of the targeted nanoparticle aggregates.

In addition to the energy-dispersive X-ray analyses, europium content was determined by inductively coupled plasma mass spectrometry (ICP-MS) on a 8800 Triple Quadrupole ICP-MS from Agilent Technologies. To do so, 10 mg of purified sample were first digested in 4 mL of trace metal grade concentrated nitric acid with the aid of an ultrasonic bath. The samples were next diluted to 100 mL with nanopure quality deionized water and analyzed by luminescence spectroscopy to confirm the release of the europium ions (see supporting information Figure S3) from the solid matrix. These solutions were then diluted to yield europium and yttrium concentrations between 0.01 - 10 µg/L and a 1 µg/L praseodymium internal standard was added. Twenty replicates were recorded per sample.

Steady-state phosphorescence was measured with a UV-VIS spectrofluorometer (Fluorolog 3-22, Horiba Jobin-Yvon). The instrument is equipped with a 450 W xenon short arc lamp, double-grating excitation and emission monochromators and a cooled Hamamatsu R928P photomultiplier tube. The emission channel has an optimal spectral response around 750 nm. Nanoparticle suspensions were prepared by dispersing 11 mg of purified sample in 10 mL of methanol using an ultrasonic bath. To prevent aggregation and sedimentation and ensure stability of the samples while acquiring the spectra, 1 mL of a 0.1 g/mL poly(ethylene glycol) methyl ether (M_n = 2000 g/mol) methanol solution was added to the suspensions and the latter were transferred to a quartz cuvette and stirred continuously during measurements using a magnetic stirring accessory. The slits were all set to a 2-nm bandwidth, the scanning increment to 1 nm and the integration time to 1 s. Emission spectra were corrected for variations in the spectral output of the excitation lamp.

Phosphorescence lifetimes were determined by Time-Correlated Single Photon Counting (TCSPC) using the T–channel of a UV-VIS-NIR spectrofluorometer (Nanolog, Horiba Jobin-Yvon). The apparatus is equipped with a double-grating emission monochromator optimized at 500 nm, a nanosecond pulsed xenon lamp as the excitation source for phosphorescence lifetime measurements, and an uncooled Hamamatsu R928 photomultiplier tube as the detector. Phosphorescence decay curves were recorded at each of the primary emission wavelengths of the europium doped nanoparticles, namely, at 592 nm, 611 nm, 619 nm, 690 nm and 699 nm. The slits were set to 2-nm or 4-nm bandwidths depending on emission line intensity. Lifetime decays were acquired with a time resolution of 21.3 µs per channel at a source repetition rate of 10 Hz, until either the most intense channel had reached 5,000 photons or the measurement period reached 6 hours. The recorded data was exported to luminescence decay data analysis software (Fluofit, Picoquant GmbH) and fitted using a single exponential tail-fit model (for the methanol solutions) or a two-exponential tail-fit model (for the europium-doped nanoparticles). In the latter case, the decay curves were either fitted separately (local fit) or by grouping decay curves for a given emission line with all 4 samples (global fit), and the amplitude-weighted lifetime was calculated as $\tau_{ave} = \sum_{i=1}^{n} A_i e^{-\frac{t}{\tau_i}}$ (n=2), with the uncertainties on A_1, τ_1, A_2, τ_2 calculated using the support plane error analysis provided by the software.

3. Results and Discussion

White nanoparticle powders with masses ranging from 250 to 500 mg were recovered as described above. The wide range of recovered-sample weight is mainly due to differences in residual surfactant levels, inadvertent losses and to the europium content. Indeed, for a fixed molar quantity of precursors, an increase in isolated sample weight should normally be expected with increasing doping levels since europium atoms are much heavier than yttrium atoms.

3.1 Particle size and shape

Transmission electron microscopy images of 5%, 10%, 15% and 20% europium-doped $(H_3O)Y_3F_{10} \cdot xH_2O$ single-crystal nanoparticles are presented in Figure 2. Depending on the orientation of the nanoparticles on the grids, different geometric shapes can be observed. These apparent shape variations result from the different possible 2D projections of regular octahedral nanoparticles and are characteristic of $(H_3O)Y_3F_{10} \cdot xH_2O$ single crystals.[16] Small amounts of residual surfactant are also visible in Figure 2 as pale, nondescript patches, present in varying quantities in the background or around some of the nanoparticles. Importantly, no elongated needle-like crystals are observed. Particles prepared by the microemulsion method described above, but starting from a 100% $EuCl_3$ 40 mM aqueous solution and no YCl_3, do not exhibit the octahedral shape characteristic of the $(H_3O)Y_3F_{10} \cdot xH_2O$ single crystals, but rather crystallize into needle-like structures (see supporting information Figure S1). Previous work realized with 40 mM (rather than 400 mM) starting reagents indicated that $(H_3O)Y_3F_{10} \cdot xH_2O$ single crystals could not be synthesized at europium doping levels above 10%. The absence of elongated particles in TEM images of Figure 2 clearly demonstrates that $(H_3O)Y_3F_{10} \cdot xH_2O$ nanoparticles can be doped with up to 20% europium without loss of the matrix crystal structure while using 400 mM starting reagents. Therefore, the concentration and the distribution of ions within the reverse micelles appear to play an important role in the nucleation and crystallization kinetics and the ultimate outcome of the synthesis.

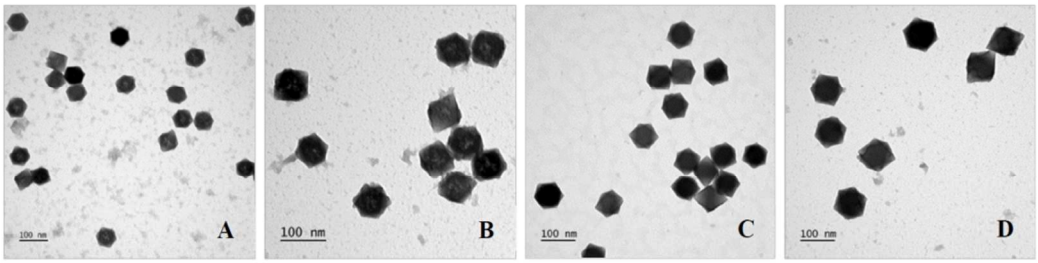

Figure 2 : Transmission electron microscopy (TEM) images showing single-crystal $(H_3O)Y_3F_{10} \cdot xH_2O$ nanoparticles doped at 5% (A), 10% (B), 15% (C) and 20% (D) with europium ions. The light gray spots present in background or around some of the nanoparticles are attributed to the presence of residual surfactant.

Size distribution histograms for the four europium-doped samples are presented in Figure 3. Particle size is defined as the distance between two opposite vertices of an octahedron, rather than the length of the edge. This dimension can be considered as the diameter of an octahedral nanoparticle while keeping in mind that it in fact corresponds to the diameter of a sphere passing through the six vertices of a regular octahedron. Size measurements are based on the approximation that all the measured nanoparticles have a regular octahedral shape and that they are perfectly positioned in the image plane. These two conditions are, however, not always fully respected, leading to apparent size distributions that are slightly broader than the true ones.

Two important observations can be noted from Figure 3. First, the size distributions are relatively narrow and broaden only slightly with increasing europium content. Secondly, the size distribution histograms systematically shift to higher values as a function of europium doping. In ascending order of doping levels, mean particle sizes of 90 ± 4 nm, 99 ± 3 nm, 103 ± 4 nm and 124 ± 6 nm are obtained. Since all four populations are synthesized at exactly the same water/surfactant molar ratio, this variation of the size is not expected. The systematic shift to larger particles indicates that europium ions do not behave exactly as yttrium ions during the nucleation process. Indeed, since the total amount of reagent is kept constant from one synthesis to another, the increasing presence of europium appears to lead to the creation of a

smaller number of nuclei, ultimately leading to the formation of larger nanoparticles. The decrease in the number of stable nuclei in the presence of europium may reflect the inability of this ion to participate in the nucleation process. As noted above, under the same microemulsion conditions, europium fluoride does not crystallize in the same form as yttrium fluoride. It is thus not unreasonable to assume that europium ions cannot contribute to the formation of nuclei that grow into octahedral nanocrystals. Since the total molar concentration remains constant, an increase in europium content corresponds to a decrease in yttrium concentration, which could be directly responsible for the reduction in the number of stable nuclei.

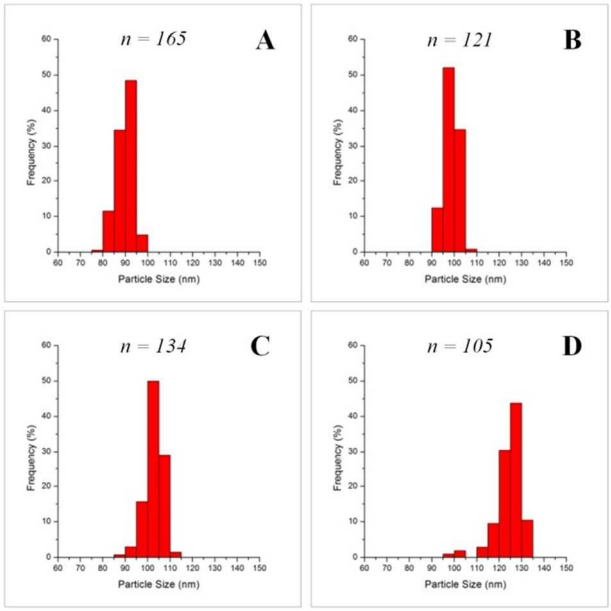

Figure 3 : Size distribution histograms of single-crystal $(H_3O)Y_3F_{10} \cdot xH_2O$ nanoparticles doped at 5% (A), 10% (B), 15% (C) and 20% (D) with europium ions. The average sizes are 90 ± 4 nm (A), 99 ± 3 nm (B), 103 nm ± 4 (C) and 124 ± 6 nm (D).

3.2 Determination of inorganic content

The TEM images of Figure 2 exhibit nondescript grey patches that are attributed to the presence of residual surfactant. This indicates that although the ultrafiltration process eliminates the large majority of the 40 g of surfactant used for nanoparticle synthesis, traces remain. Thermogravimetric analyses were performed to determine the true inorganic content of each of the purified sample. Results are shown in Figure 4.

As shown in Figure 4, all samples demonstrate weight loss in the temperature range of 50 to 500 °C. Generation of H_2O and CO_2 decomposition products, followed by mass spectrometry (MS) at mass-to-charge ratios (m/z) of 18 and 44, respectively, shows that initial weight losses correspond to the removal of zeolitic water contained in the $(H_3O)Y_3F_{10} \cdot xH_2O$ nanoparticles. The appearance of CO_2 at approximately 300 °C suggests that from this temperature on, weight loss is mainly caused by decomposition of residual surfactant molecules (see supporting information Figure S2). More importantly, stabilization of the sample weight around 525 °C demonstrates that at this temperature and above all volatile and organic compounds have been removed. Thus, for each sample, the weight recorded at 600 °C was attributed to the inorganic content and, in ascending order of doping levels, corresponds to 75.8%, 84.2%, 82.6% and

83.2% of the total sample mass. These values were subsequently employed to correct data collected by ICP-MS and luminescence spectroscopy.

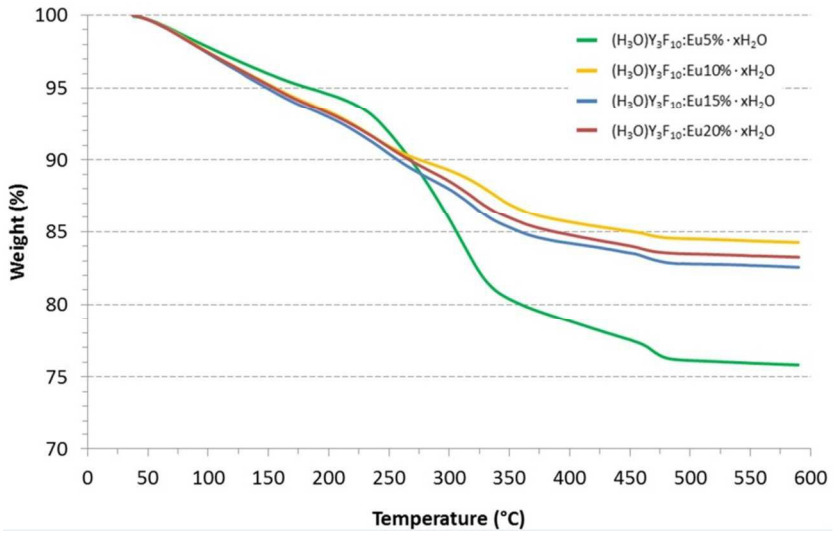

Figure 4 : Thermogravimetry curves of single crystal $(H_3O)Y_3F_{10} \cdot xH_2O$ nanoparticles. Analysis was performed on samples purified by ultrafiltration and doped with 5% (green), 10% (yellow), 15% (blue) and 20% (red) europium ions.

3.3 Determination of the europium-doping level

Since it cannot be assumed that the dopant ions are completely incorporated during crystallization, it is important to determine the actual europium doping levels in the final nanoparticles. Two methods of analysis were employed, EDX spectroscopy and ICP-MS. Initially, EDX analysis was employed as an attempt to evaluate the elemental composition of individual nanoparticles in order to obtain information about possible particle-to-particle variations in doping. Unfortunately, this technique was found to not be sensitive enough to analyze single nanoparticles. Ensemble elemental compositions could, however, be determined from nanoparticle aggregates of several microns in size. Two nanoparticle aggregates were analyzed per sample and the resulting elemental compositions are tabulated in Table S1 of the supporting information. The mean europium doping levels, calculated from the Eu/Y ratios, are plotted in Figure 5 as a function of the theoretical doping level (i.e. that calculated from initial reactant ratios).

The results presented in Figure 5 show that the actual doping level falls below the ideal one for each of the nanoparticle populations, suggesting that europium incorporation is incomplete. Since it is also possible that the lower-than-expected europium contents are the result of a systematic error inherent to the analytical technique, the europium doping levels were also determined by ICP-MS (see supporting information Figure S4). The doping levels determined these two different techniques are reported in Table S2 of the supporting information. Even though the ICP-MS values have greater associated uncertainties than those determined by EDX spectroscopy, there is very good agreement between the results obtained by the two methods. First, both techniques demonstrate that the final europium doping level increases as the fraction of $EuCl_3$ in the initial precursor chloride mixture is increased from 5 to 20%. Furthermore, both techniques indicate that the actual europium doping level systematically falls below the theoretical one. This demonstrates that europium ions are less readily incorporated into the $(H_3O)Y_3F_{10} \cdot xH_2O$ crystal lattice than are yttrium ions.

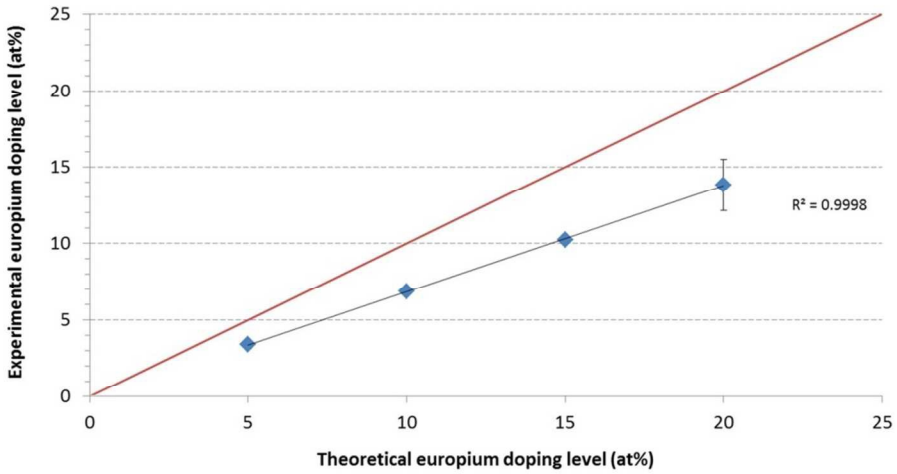

Figure 5 : Europium doping levels of $(H_3O)Y_3F_{10} \cdot xH_2O$ nanoparticle samples determined by energy-dispersive X-ray spectroscopy and compared with theoretical doping levels. Red line represents ideal case where the experimental doping level is equal to the theoretical one (i.e. calculated from initial reactant ratios). Error bars correspond to the standard deviation (n=2).

3.4 Characterization of the spectral properties

The excitation and emission spectra of a methanol suspension of $(H_3O)Y_3F_{10}$:Eu20% $\cdot xH_2O$ single-crystal nanoparticles are shown in Figure 6. For comparison, the excitation and emission spectra of an aqueous and a methanol solution of europium nitrate are also provided. The observed excitation and emission peaks can be assigned to known Eu^{3+} transitions as shown.[19] Significantly, the relative intensities of the various emission peaks vary from one spectrum to the other. It is plausible that different pathways for non-radiative energy loss exist for solvated ions free in solution than for ions embedded in the crystalline matrix, pathways that may affect some radiative transitions more than others.

Furthermore, comparison of the three emission spectra presented in Figure 6 indicates the impact of the yttrium fluoride lattice on the phosphorescence spectrum of the europium ions, thus validating their incorporation into the single-crystal $(H_3O)Y_3F_{10} \cdot xH_2O$ nanoparticles. Indeed, the emission spectrum of the $(H_3O)Y_3F_{10}$:Eu20% $\cdot xH_2O$ nanoparticle suspension presents a much more significant splitting of the $^5D_0 \rightarrow {}^7F_2$ and $^5D_0 \rightarrow {}^7F_4$ transitions than either of the europium nitrate solutions. This characteristic splitting of the emission transitions is caused by the crystal field effect. Obviously, the latter phenomenon is much more important in the case of the europium doped nanoparticles. This is simply because the luminescent ions incorporated into the yttrium fluoride crystals are more strongly coordinated than those in solution. As a result, the degeneracy of the ^7F_J levels of the europium ions located into the yttrium fluoride nanoparticles is more intensely broken and an important splitting of the emission peaks can be observed.

Excitation-emission spectra of the 5%, 10%, 15% and 20% europium-doped nanoparticles suspensions are shown in Figure 7. The emission spectra of all of the samples show similar relative intensities and crystal-field splitting characteristic of Eu^{3+} incorporated in $(H_3O)Y_3F_{10} \cdot xH_2O$ nanocrystals. Furthermore, the emission intensities increase linearly with increasing europium doping, as demonstrated in Figure 8. Importantly, no loss in emission intensity from self-quenching is observed, suggesting that even more intense phosphorescence could be obtained by further doping the nanoparticles.

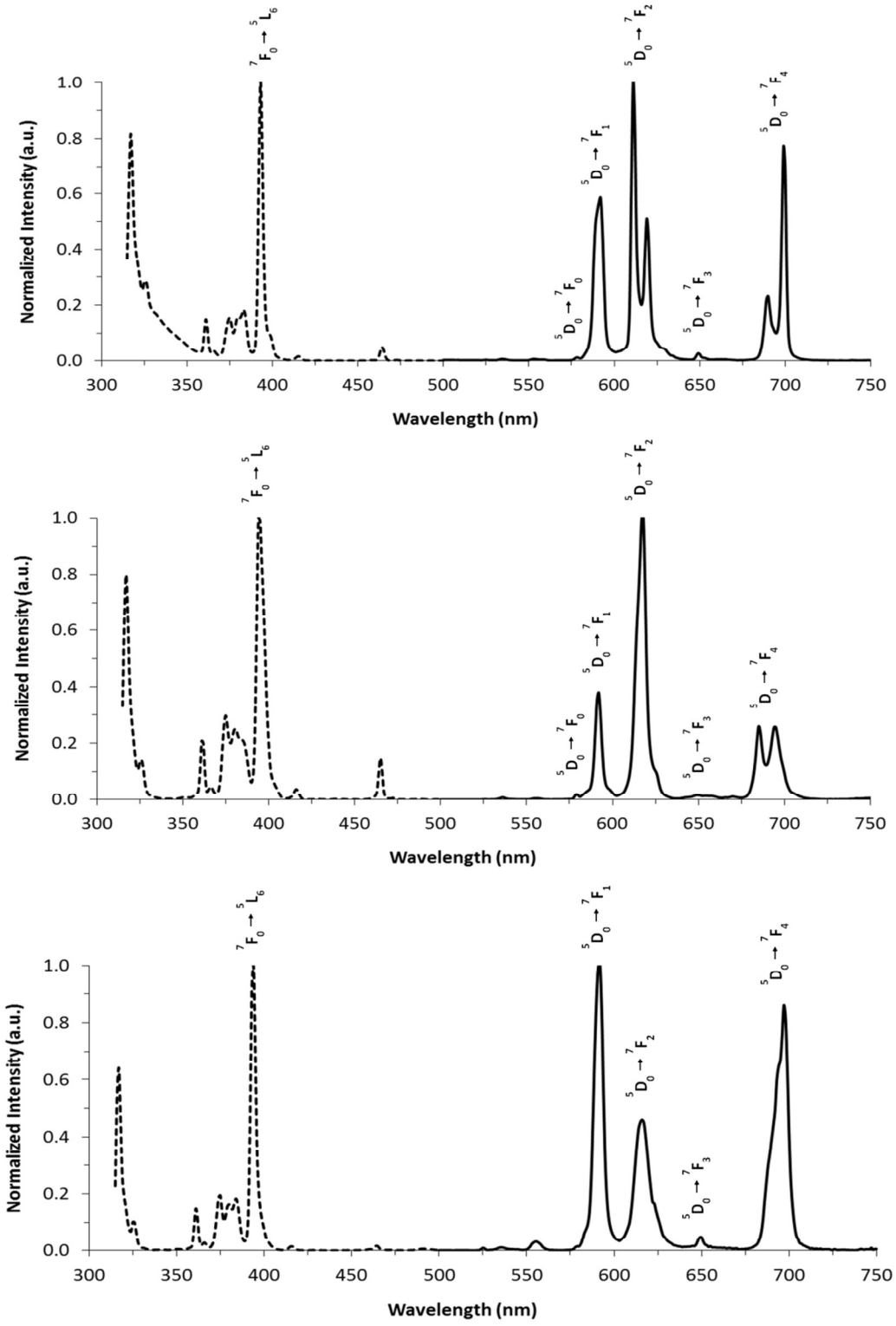

Figure 6 : Excitation (dashed line; λ_{em} = 611, 617 and 592 nm from top to bottom) and emission (solid line; λ_{exc} = 393 nm) spectra of methanol suspension of $(H_3O)Y_3F_{10}$:Eu20% · xH_2O nanoparticles (top), methanol solution of europium nitrate (middle) and aqueous solution of europium nitrate (bottom).

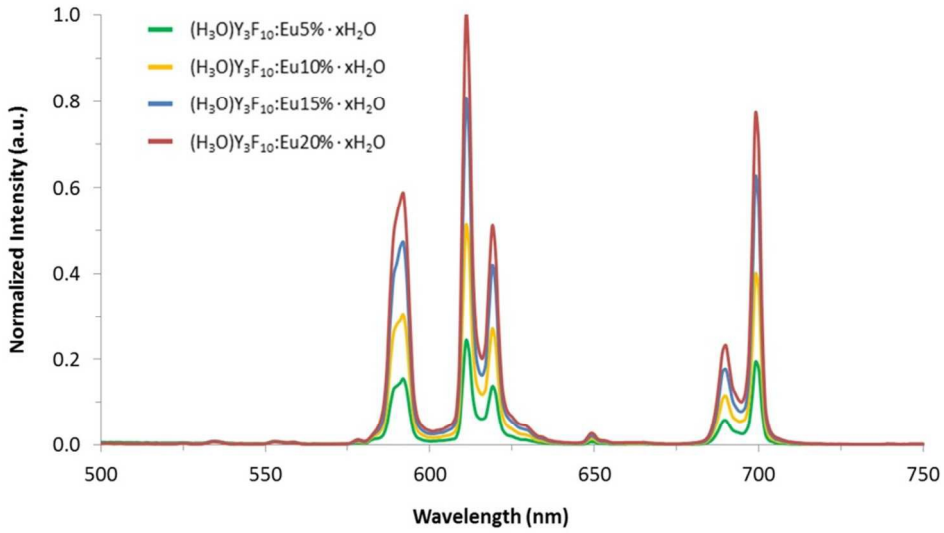

Figure 7 : Emission spectra (λ_{exc} = 393 nm) of methanol suspensions of single crystal $(H_3O)Y_3F_{10} \cdot xH_2O$ nanoparticles doped at 5% (green), 10% (yellow), 15% (blue) and 20% (red) with europium ions.

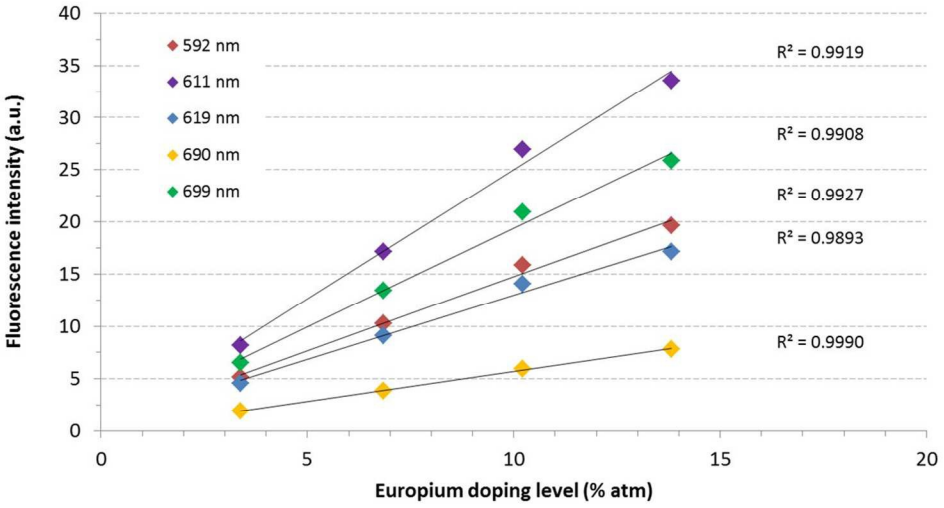

Figure 8 : Emission intensity of single crystal $(H_3O)Y_3F_{10} \cdot xH_2O$ nanoparticles doped at 5%, 10%, 15% and 20% with europium ions recorded at 592 nm (red), 611 nm (purple), 619 nm (blue), 690 nm (yellow) and 699 nm (green). (λ_{exc} = 393 nm)

The doped nanoparticles were also studied by time-resolved phosphorescence spectroscopy. Compared to organic fluorophores, luminescent ions such as europium have phosphorescence spectra that are characterized by sharp excitation and emission peaks. Excited-state lifetimes can thus be independently measured for different emission transitions. Here, luminescent decay curves were recorded for each europium-doped nanoparticle suspension (5%, 10%, 15% and 20%) at emission lines 592 nm, 611 nm, 619 nm, 690 nm and 699 nm, as well as for a 8-mM methanol solution of europium nitrate at 591 nm, 616 nm, 684 nm and 694 nm (see Tables S3 to S5 for detailed lifetime data for all samples and transitions). As expected, the appearance of the recorded decay curves differs significantly for both types of samples, the decay curves recorded with the methanol solution exhibiting a classical single exponential character (Figure S5), indicative of an homogeneous environment, whereas the presence of more than one decay

time is evident from the curvature in the semi-log signal plots recorded for the europium-doped nanoparticles (Figure S6). Consequently, excited-state lifetime values for the nanoparticles were extracted from the decay curves using a double-exponential tail-fit model. Figure 9 shows short and long decay components of the excited state lifetimes for all five emission lines with the 20% europium-doped nanoparticles, as well as for the four lines recorded with the methanol solution of europium nitrate. Interestingly, the excited-state lifetimes for the methanol solution are approximately 10 times shorter than for the doped nanoparticles, an indication that the yttrium fluoride lattice of the latter is efficiently protecting the europium ions from quenching effects.

The inability to fit the decay curves to a single exponential reflects the existence of more than one emitting site within the nanocrystals. In fact, ^{19}F-^{89}Y VACP/MAS NMR experiments carried out on non-doped $(H_3O)Y_3F_{10} \cdot xH_2O$ nanoparticles clearly indicated the presence of two distinct ^{89}Y sites.[18] The variation of the relative abundance of these sites with particle size suggests that one is located on or near the nanoparticle surface whereas the second one is located deeper in the nanoparticle core. Consequently, it is reasonable to assume that at least two distinct europium sites (and probably more than two) must also be present in the europium-doped yttrium fluoride nanoparticles investigated in this work. Since spectral properties such as transition probabilities are highly dependent on the site symmetry in which the lanthanides ions are located, these different europium "species" can be considered as being spectroscopically different and could result in the double exponential decay profiles that we observed. Furthermore, europium ions located at the surface will be susceptible to quenching by solvent molecules or residual surfactant. To ascertain this hypothesis, the decay data was examined by global analysis,[20] based on the assumption that the value of the short and long decay components are independent of doping level, with only their relative amplitude varying between samples. Therefore, fitting all decay curves from each line and all four samples and by setting lifetime components τ_1 and τ_2 as global parameters (independent of europium concentration), one obtains different amplitude values for each data set that reflect the relative contribution of each site to the overall excited state lifetime. Figure 10 shows the values of the pre-exponential term (amplitude A_2) for the short lifetime component τ_2 calculated for the 592, 611 and 619 nm emission lines and plotted as a function of doping level. For all three emission lines, the results show that the amplitude correlates well with the average nanoparticle size (Figure 3), with a significant increase in size between the samples with 5% and 20% nominal doping levels but only a slight increase between the 10% and 15% samples. Furthermore, this global analysis yields remarkably similar values independent of doping level and wavelength for the long lifetime component – which presumably corresponds to the sites buried within the crystalline matrix and away from the nanoparticle surface – whereas the amplitude-weighted average lifetime τ_{ave} decreased with doping level for all emission lines (see Table S4). These results can be explained through variations in the relative population of these sites. As noted above, particle size variations and incomplete europium incorporation indicate that Y^{3+} and Eu^{3+} are not added to the growing nanocrystals with the same probability. This means that the Eu^{3+}/Y^{3+} free ion ratio increases throughout the growth process and doping levels may increase from the center to the surface of the final particles. The fraction of Eu^{3+} ions occupying surface sites can therefore be predicted to increase with increasing doping levels.

Another feature of interest revealed by this study is the measurement of different lifetimes from different emission lines. Whereas almost identical lifetime values are recorded from one wavelength to another for the methanol solution, perceptibly different lifetimes are recorded for different transitions in the case of the nanoparticles. Since the transitions responsible for the different emission lines all originate in the $^5D_0$ excited state of the trivalent europium ion and since the effective lifetime measured for this excited state is affected by all radiative and non-radiative relaxation pathways available, the lifetime of this excited state should be independent of the radiative pathway used to measure it. In other words, lifetimes determined for the emission lines listed above should all yield identical values, as is the case for the europium nitrate solution. The differences in excited-state lifetime observed for the europium-doped nanoparticles, particularly in the value of the short decay component for the emission lines with the strongest signal to noise ratio (592, 611 and 619 nm), exceed the uncertainty associated with the measurement method and, to the best of our knowledge, are not caused by experimental error. These variations may suggest the presence more than one type of *surface* site, characterized by different lifetimes and different emission probabilities. Although for a given sample, the relative population of spectroscopically distinct surface sites would be constant, their relative contribution to emission intensity can vary from one wavelength to another. In this way, heterogeneity in the surface sites would lead to variations in the short luminescence lifetime as determined from different emission lines. Although this explanation is somewhat speculative, the existence of a number of different surface sites is highly probable.

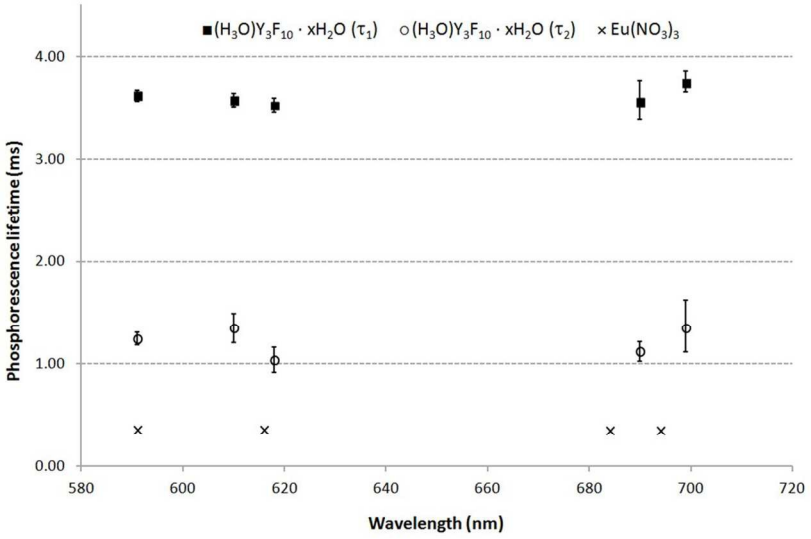

Figure 9: Phosphorescence long (■) and short (○) decay lifetime components for a methanol suspension of single crystal $(H_3O)Y_3F_{10} \cdot xH_2O$ nanoparticles doped at 20% with europium ions (×: single-exponential decay lifetime of a 8-mM methanol solution of europium nitrate) (λ_{exc} = 393 nm).

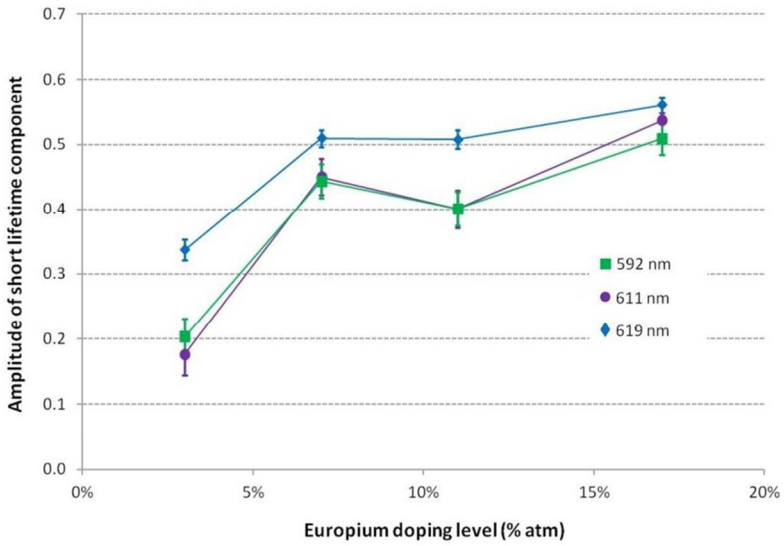

Figure 10: Amplitude of short lifetime component calculated with a two-exponential global tail-fit for $(H_3O)Y_3F_{10} \cdot xH_2O$ nanoparticles as a function of europium doping level.

4. Conclusions

Single nanocrystals of $(H_3O)Y_3F_{10} \cdot xH_2O$ can be doped with europium to yield luminescent particles. Importantly, dopant levels of 14 mol % can be reached without loss of the matrix crystal structure. The emission spectra of the doped nanoparticles show sharp well-defined lines, which can be assigned to known europium transitions. The relative intensities of the various bands in the nanoparticle spectra differ significantly from those observed from europium ions in solution. Furthermore, steady-state phosphorescence measurements indicate that the nanoparticle emission increases linearly with europium doping levels.

Time-resolved phosphorescence measurements reveal unexpected variations in excited-state lifetimes. Different lifetimes are recorded for various transitions, despite the fact that they all originate in a common excited state. In addition, different lifetimes are recorded for nanoparticles with different doping levels. These results are tentatively explained by the existence of distinct and spectroscopically different europium sites, distributed between the bulk of the $(H_3O)Y_3F_{10}{\cdot}xH_2O$ nanoparticles and the particle surface. This interpretation is concordant with previous solid state NMR results[18] and two observations related to synthesis conditions; namely, that particle size increases with increased doping concentration and final doping levels are lower than the molar ratio of ions in the precursor solutions. Comparison of phosphorescence lifetimes of free europium ions in solution and europium-doped $(H_3O)Y_3F_{10}{\cdot}xH_2O$ single-crystal suspensions show that the crystal lattice efficiently protects the europium ions from the external environment and its quenching effects.

These particles exhibit luminescent properties that make them potentially interesting candidates as probes in detection or imaging applications. Furthermore, this study shows that the delineation of photophysical processes in such materials requires access to uniform, well-defined particle populations.

Acknowledgements

The authors would like to acknowledge le Fonds de recherche du Québec – Nature et technologies (FRQNT), the National Sciences and Engineering Research Council of Canada (NSERC) and the Canadian Foundation for innovation (CFI) for financial support. They also thank Maxime Blanchette for useful discussions, Nima Masoumifard for his contribution to TGA-MS measurements, Charles Labrecque for assistance with ICP-MS, and Jérémie Asselin for help with the time-resolved phosphorescence characterization.

Associated Content

Supporting Information

Additional information is available via the Internet at …

Author information

Corresponding Author

E-mail : Anna.Ritcey@chm.ulaval.ca

References

[1] Elbanowski, M.; Makowsaka, B., The lanthanides as luminescent probes in investigations of biochemical systems. *Journal of Photochemistry and Photobiology a-Chemistry* **1996,** *99* (2-3), 85-92.

[2] Bouzigues, C.; Gacoin, T.; Alexandrou, A., Biological Applications of Rare-Earth Based Nanoparticles. *Acs Nano* **2011,** *5* (11), 8488-8505.

[3] Jadhav, A. P.; Kim, C. W.; Cha, H. G.; Pawar, A. U.; Jadhav, N. A.; Pal, U.; Kang, Y. S., Effect of Different Surfactants on the Size Control and Optical Properties of Y2O3:Eu3+ Nanoparticles Prepared by Coprecipitation Method. *Journal of Physical Chemistry C* **2009,** *113* (31), 13600-13604.

[4] Yu, L. X.; Song, H. W.; Lu, S. Z.; Liu, Z. X.; Yang, L. M.; Kong, X. G., Luminescent properties of LaPO4 : Eu nanoparticles and nanowires. *Journal of Physical Chemistry B* **2004,** *108* (43), 16697-16702.

[5] Taniguchi, T.; Soga, K.; Tokuzen, K.; Tsujiuchi, K.; Kidokoro, T.; Tomita, K.; Katsumata, K.-i.; Matsushita, N.; Okada, K., NIR-excited NIR and visible luminescent properties of amphipathic YVO4: Er3+/Yb3+ nanoparticles. *Journal of Materials Science* **2012,** *47* (5), 2241-2247.

[6] Li, C. X.; Lin, J., Rare earth fluoride nano-/microcrystals: synthesis, surface modification and application. *Journal of Materials Chemistry* **2010,** *20* (33), 6831-6847.

[7] Diamente, P. R.; van Veggel, F., Water-soluble Ln(3+)-doped LaF3 nanoparticles: Retention of strong luminescence and potential as biolabels. *Journal of Fluorescence* **2005,** *15* (4), 543-551.

[8] Wang, F.; Zhang, Y.; Fan, X. P.; Wang, M. Q., Facile synthesis of water-soluble LaF3 : Ln(3+) nanocrystals. *Journal of Materials Chemistry* **2006,** *16* (11), 1031-1034.

[9] Zhuravleva, N. G.; Sapoletova, N. A.; Eliseev, A. A.; Lukashin, A. V.; Tretyakov, Y. D.; Kynast, U., The synthesis of monodisperse trioctylphosphine oxide-capped EuF3 nanoparticles. *Optical Materials* **2006,** *28* (6-7), 606-609.

[10] Diamente, P. R.; Raudsepp, M.; van Veggel, F. C. J. M., Dispersible Tm3+-doped nanoparticles that exhibit strong 1.47 mu m photoluminescence. *Advanced Functional Materials* **2007,** *17* (3), 363-368.

[11] Vinny R. Sastri,J.R. Perumareddi,V. Ramachandra Rao,G.V.S. Rayudu,J.-C. G. Bünzli, Modern Aspects of Rare Earths and their Complexes, 1st Edition, Elsevier Science, 09 Dec 2003, p 93.

[12] Mahalingam, V.; Vetrone, F.; Naccache, R.; Speghini, A.; Capobianco, J. A., Colloidal Tm3+/Yb3+-Doped LiYF4 Nanocrystals: Multiple Luminescence Spanning the UV to NIR Regions via Low-Energy Excitation. *Advanced Materials* **2009,** *21* (40), 4025-+.

[13] Bogdan, N.; Vetrone, F.; Ozin, G. A.; Capobianco, J. A., Synthesis of Ligand-Free Colloidally Stable Water Dispersible Brightly Luminescent Lanthanide-Doped Upconverting Nanoparticles. *Nano Letters* **2011,** *11* (2), 835-840.

[14] Ma, M.; Yang, L.; Ren, G.; Xu, C.; Lin, J.; Yang, Q., Solvothermal synthesis, cubic structure and multicolor upconversion emission of ultrasmall monodisperse lanthanide-doped BaYF5 nanocrystals. *Journal of Luminescence* **2011,** *131* (7), 1482-1486.

[15] Li, C.; Mei, Y.; Xie, J.; Dai, W.; Du, G.; Li, Z., Controlled synthesis of YF3 nanocrystals with multiple morphologies in ethylene glycol. *Journal of Alloys and Compounds* **2013,** *560*, 10-14.

[16] Lemyre, J. L.; Ritcey, A. M., Synthesis of lanthanide fluoride nanoparticles of varying shape and size. *Chemistry of Materials* **2005,** *17* (11), 3040-3043.

[17] Lemyre, J. L.; Lamarre, S.; Beaupre, A.; Ritcey, A. M., Mechanism of YF3 Nanoparticle Formation in Reverse Micelles. *Langmuir* **2011,** *27* (19), 11824-11834.

[18] Lucier, B. E. G.; Johnston, K. E.; Arnold, D. C.; Lemyre, J.-L.; Beaupre, A.; Blanchette, M.; Ritcey, A. M.; Schurko, R. W., Comprehensive Solid-State Characterization of Rare Earth Fluoride Nanoparticles. *Journal of Physical Chemistry C* **2014,** *118* (2), 1213-1228.

[19] Karunakaran, R. T.; Marimuthu, K.; Babu, S. S.; Arumugam, S., Structural, optical and thermal studies of Eu3+ ions in lithium fluoroborate glasses. *Solid State Sciences* **2009,** *11* (11), 1882-1889.

[20] Knutson, J. R.; Beecham, J. M.; Brand, L., Simultaneous analysis of multiple fluorescence decay curves: a global approach. *Chemical Physics Letters* **1983**, *102* (6), 501-507.